Measurement of interfacial Dzyaloshinskii-Moriya interaction from static domain imaging

Parnika Agrawal, Felix Büttner, Ivan Lemesh, Sarah Schlotter, and Geoffrey S. D. Beach

Phys. Rev. B **100**, 104430 — Published 23 September 2019

DOI: 10.1103/PhysRevB.100.104430

Measurement of interfacial Dzyaloshinskii-Moriya interaction from static domain imaging

Parnika Agrawal[1], Felix Büttner[1], Ivan Lemesh[1], Sarah Schlotter[1,2], and Geoffrey S. D. Beach[1]

[1]Department of Materials Science and Engineering, MIT

[2]John A. Paulson School of Engineering and Applied Sciences, Harvard University

Abstract

Perpendicularly magnetized thin films with strong Dzyaloshinskii-Moriya interaction (DMI) exhibit chiral spin structures such as Néel domain walls and skyrmions. These structures are promising candidates for next generation magnetic memory devices. Determining the magnitude of DMI accurately is key to engineering materials for such applications. Existing approaches are based either on quantities extracted from magnetization dynamics, which presents experimental and theoretical challenges, or from measurements of quasistatic domain spacing, which so far have been analyzed using incomplete models or prohibitively slow micromagnetic simulations. ~~Here, we show that extraction of DMI from domain spacing can be done rapidly, accurately, and self-consistently provided the domain wall energy in chiral systems is accurately accounted for. Specifically, we show that DMI can be obtained from measurement of the magnetic domain width in the demagnetized state, the perpendicular anisotropy constant, and the saturation magnetization. We extract DMI from domain width measurements in micromagnetically simulated films within a 1% error margin. Additionally, we show that our model can be used to estimate the error in the extracted DMI based on its relative strength compared to the exchange and magnetostatic energies in the system. We provide a simple and robust tool to determine the~~

~~DMI strength of a material system with significant DMI, that falls into a multidomain state, as we demonstrate experimentally for a thickness-graded multilayer magnetic film.~~ Here, we use a recently developed analytical model of stripe domain widths in perpendicularly magnetized multilayers to extract the DMI from domain images combined with magnetometry data. Our approach is tested on micromagnetically simulated domain patterns, where we achieve a 1% agreement of the extracted DMI with the DMI used to run the simulation. We then apply our method to determine the thickness-dependent DMI in two experimental materials, one with ([Pt(2.5 - 7.5 nm)/$Co_{60}Fe_{20}B_{20}$(0.8 nm)/MgO(1.5 nm)]$_{13}$) and one without ([Pt(2.5 - 7.5 nm)/Co(0.8 nm)/Pt(1.5 nm)]$_{13}$) inversion symmetry breaking. We discuss the means to obtain realistic error bars with our method. Our results demonstrate that analytical domain spacing analysis is a powerful tool to extract DMI from technologically relevant multilayer materials.

1 Introduction

Chiral spin textures, such as homochiral domain walls (*1*, *2*) and skyrmions (*3*, *4*), have been found in materials with sizable perpendicular magnetic anisotropy (PMA) and Dzyaloshinskii-Moriya interaction (DMI), where those interactions are generated at heavy-metal/ferromagnet interfaces. Typically, the DMI alone is insufficient to break the homogeneous out-of-plane spin state favored by anisotropy and exchange. However, when stacked to ~~In asymmetric~~ multilayers, the demagnetizing energy helps to break the uniform magnetization state into multiple stripe or labyrinth domains. These stripe and labyrinth domains have been found to be useful in creating skyrmion lattices in thin-film heterostructures (*5–8*). Quantifying the DMI in such films accurately and reliably is of critical importance for identifying potential materials for skyrmion-based devices.

First principle calculations (*9*, *10*) have been used to predict the origin and materials dependence of DMI at thin-film interfaces, but systematic experimental studies for comparison are hindered by a lack of techniques that are simple to perform and interpret. Most experimental estimates of DMI have been derived from dynamics, including field-driven (*11*) or current-driven (*1*) domain wall motion, or asymmetries in the spin wave spectrum (*12*, *13*). However, domain wall dynamics studies require many assumptions and are often ambiguous (*14–16*), particularly

the common bubble-expansion experiments in which the detailed pinning landscape and associated domain wall energies and creep parameters are challenging to model (*17*). Spin wave studies are more straightforward to analyze and interpret, but are usually only practical in materials with low damping (*18*). All of these methods are limited in their applicability since sophisticated experiments must be performed, sometimes requiring device patterning into, e.g., racetracks (*2*).

An alternative technique is based on domain spacing measurements in the equilibrium state, which is determined by minimization of the total energy including demagnetizing and domain wall energies (*5*, *7*). Since most micromagnetic parameters can be determined by conventional magnetometry, measurement of the domain spacing can be used to determine the domain wall energy, which allows the DMI to be estimated with very few assumptions. The advantages of extracting DMI from domain spacing as opposed to magnetization dynamics are that it only requires that the samples be prepared in a global energy minimum demagnetized state, i.e., a state in which the domain width is determined by competing magnetic energies and not by nucleation or pinning. There are no restrictions on the shape of the hysteresis loop as long as there is PMA. The domains should be ~~large enough~~ of suitable size to be measured in standard domain imaging tools such

as magnetic force microscopy (MFM), transmission x-ray microscopy (STXM), small angle x-ray scattering (SAXS), or similar techniques. ~~Although~~ Several prior works (*5*, *7*) have used domain spacing analyses to extract DMI in thin-film multilayers. However, on the one hand, Ref. (*5*) ~~relied on inaccurate~~ has used oversimplified expressions for domain wall energy based on approximations that have recently been shown to lead to considerable quantitative errors, particularly in chiral systems ~~of interest~~ with Néel domain walls (*19*). Moreau-Luchaire et al. (*7*), on the other hand, made an attempt to extract DMI by comparing to micromagnetic simulations, which is a slow and inefficient process. Moreover, error estimates on the extracted DMI are hard to obtain unless every magnetic parameter is varied separately in simulations which would be even slower. In this work, we use an analytical model for the energy density of a stripe domain state, which yields the equilibrium domain widths almost instantaneously. We use this model to determine the DMI strength corresponding to the measured domain widths. We highlight the importance of using the most accurate domain wall energy model (*19*) since simpler conventional models lead to ~~importance of using the full domain wall energy model, and show that only the complete model allows accurate extraction of DMI. We show that when analyzed with commonly-used models, the DMI values obtained can show~~ considerable quantitative error. We

then experimentally demonstrate that the accurate domain wall energy model can be used to ~~accurate and self-consistently analyze and~~ extract DMI in multilayer films with a continuous thickness gradient. By analyzing multilayer films with thickness gradients, we demonstrate that consistent fitting can be obtained across a wide range of material properties using only a few free parameters. The experimental data reveal that the anisotropy and DMI in such films scales in a more complex way than a simple inverse-thickness behavior, which has practical importance in the interpretation of experiments in such systems.

2 Analytical models for out-of-plane stripe domains

In this section, we compare the key features of various analytical models for out-of-plane stripe domains and estimate DMI in a micromagnetically simulated multilayer magnetic film using these models. The earliest model predicting domain size in perpendicularly magnetized thin films with Bloch domain walls was developed by Kittel (*20*) and extended to multi-layers by others (*21–24*). It assumes domain walls to be sharp, i.e., it approximates the domain wall width, Δ, to be 0. Correction to this model for Néel domain walls was suggested (*25*) in the form of an extra domain wall transverse anisotropy term, $K_{\perp}$, which includes effects of

DMI and volume charges inside Néel walls. In the case of films with significant DMI and Néel walls, the effects of finite domain wall width were further introduced with a revised analytical model (*19*), whose accuracy was demonstrated by comparing extensively with full micromagnetic simulations. According to this model, the total energy per unit volume, $\mathcal{E}_{tot}$, of a demagnetized magnetic multilayer film is given by

$$\mathcal{E}_{tot} = \frac{1}{d}\left[\frac{2A_{ex}}{\Delta} + 2K_U\Delta + \pi D\text{sin}(\psi)\right] + \mathcal{E}_s + \mathcal{E}_v + \frac{\mu_0 M_S^2}{2}(f - f^2) \quad (1)$$

where $\mathcal{E}_s$ and $\mathcal{E}_v$ are the surface and volume stray field energies per unit volume, respectively given by

$$\begin{aligned}\mathcal{E}_s &= \frac{\pi\mu_0 M_S^2 f^2\Delta^2}{dt}\sum_{n=1}^{\infty}\left[\frac{\text{sin}^2\left(\frac{n\pi}{2}\right)}{\text{sinh}^2\left(\frac{\pi^2 n\Delta}{2d}\right)}\frac{1-\text{exp}(-\frac{\pi nt}{d})}{n}\right], \text{ and} \\ \mathcal{E}_v &= \frac{\pi\mu_0 M_S^2 f^2\Delta^2}{dt}\text{sin}^2(\psi)\sum_{n=1}^{\infty}\left[\frac{\text{sin}^2(\frac{n\pi}{2})}{\text{cosh}^2\left(\frac{\pi^2 n\Delta}{2d}\right)}\frac{\text{exp}\left(-\frac{\pi nt}{d}\right)+\frac{\pi nt}{d}-1}{n}\right].\end{aligned} \quad (2)$$

The surface stray field energy, $\mathcal{E}_s$, is the stray field in a magnetic film with stripe domains and finite domain wall width, Δ. The volume stray field energy, $\mathcal{E}_v$, is the energy in the stray field interactions between volume charges in the Néel domain walls of the magnetic film. In these equations, M_S is the saturation magnetization, d is the stripe domain width, t is the thickness of the magnetic film, K_U is the uniaxial anisotropy, Δ is the domain wall width, A_{ex} is the exchange constant and f is the scaling factor defined as the ratio of thickness of each magnetic

layer to the multi-layer period (as shown in Figure 1). Extraction of the domain wall energy from equilibrium domain spacing, d, hence can be used to extract the DMI strength D, as long as the other magnetic parameters are known through, e.g., conventional magnetometry.

We first highlight the errors introduced by earlier, simplified domain wall energy models by applying analytical domain spacing analysis to micromagnetically computed domain images based on known input material parameters. Simulations were performed using the MUMAX^3 software package (*26*). Similar to multilayer-films that have previously been used to realize skyrmions (*5–7*) and to the films used in experiments below, our simulations used the following magnetic and structural parameters: saturation magnetization, $M_S = 7 \times 10^5$ A/m, exchange constant, $A_{ex} = 10^{-11}$ J/m, uniaxial anisotropy energy, $K_U = 5 \times 10^5$ J/m^3, thickness of each magnetic layer, T = 0.9 nm, number of repeats, $N = 15$, and DMI constant, D = 1 mJ/m^2. The scaling factor, f, was varied from 0.1 to 0.3, corresponding to the range in the experiments described later in this work. The cell size chosen for the simulations is 2 nm $\times$ 2 nm $\times$ thickness of the film. The lateral dimensions of the simulation cell are chosen to be a few times smaller than the domain wall width for the magnetic film simulated, which in this case is $\Delta \sim$ 6 nm. Figure 1 shows a schematic of a perpendicularly magnetized multilayer thin

film with stripe domains with key thicknesses highlighted. The initial magnetization state in the simulations was chosen to be random. The magnetization was then relaxed at zero external fields and the equilibrium labyrinth domain width in the relaxed magnetic contrast images was extracted by taking a Fourier transform (FT). Figures 2a, b show 5×5 μm^2 simulated out-of-plane magnetization images after relaxation at scaling factors, $f = 0.3$ and $f = 0.1$, respectively. Figures 2c, d show the FT of the domain patterns in Figures 2a, b, respectively. The FT intensity was radially averaged and the peak was fit to a Gaussian function, as shown in Figures 2e, f for scaling factors, $f = 0.3$ and $f = 0.1$, respectively. The domain spacing, d, was calculated as half of the period obtained from the inverse of the peak frequency in FT. The variation of domain size thus obtained with f, and the least square fit of the data with the three stripe domain models described earlier is shown in Figure 2g. The error bars on the simulated data correspond to the uncertainties in the Gaussian fit to the radially averaged intensity of the FT (Figures 2e, f). For larger domains, as in Figure 2b, the errors in domain sizes are higher since there are fewer domains in the simulated image, thereby making the Gaussian peak broader.

Specifically, we show the degree of inaccuracy in measurement of DMI through the use of the following 3 models: Model 1 is the original stripe-domain model

(*20–24*) developed for single- and multi-layered films of intermediate thicknesses with PMA and Bloch domain walls. It assumes the domain walls to be sharp,i.e., $\Delta = 0$. Model 2 is a modification of model 1 for Néel domain walls and includes the domain wall transverse anisotropy, $K_\perp$ (*25*). The surface stray field energy still assumes infinitely sharp walls but the domain wall energy now includes the effects of DMI and volume charges inside Néel walls. Model 3 is built upon model 2 to also include effects of finite domain wall width, Δ, and interactions of volume charges between different Néel domain walls (*19*). Moreover, this model incorporates the film thickness dependence of the domain wall width, Δ, and the domain wall angle, ψ.

While a good fit is obtained with all models, the DMI values obtained from the three models are very different. The blue curve in Figure 2g shows a fit to the isolated domain wall approximation that does not include the effect of volume charges in the domain wall via $K_\perp$ (model 1). It gives a very small value of D = 0.28 mJ/m^2. The green curve shows the fit obtained from using model 2 and gives a 6% error in estimation of DMI. This does not include the effect of a finite domain wall width Δ but includes effects of volume charges within domain walls via $K_\perp$. The red curve is the most accurate fit (model 3) with only 1% error. Note that this was a one parameter optimization with the DMI constant, D, as the only

fitting parameter. Thus, we show that if all other parameters of the film are known accurately, model 3 gives the DMI value to within 1% of the actual value. We therefore use model 3 for the remainder of the paper.

Next, we show in Figure 3 how uncertainties in the determination of various material parameters impact the value of the extracted DMI and its error bars for commonly studied magnetic films for skyrmion applications (*5–7*). For this analysis, we choose film parameters similar to the micromagnetic simulations: M_S = 7×10^5 A/m, $A_{ex} = 10^{-11}$ J/m, $K_U = 5 \times 10^5$ J/m^3, T = 0.9 nm, multilayer periodicity λ = 4.9 nm, and N = 15. The general trend is for d to decrease with increasing DMI, D, due to the reduction in domain wall energy. The gray regions denote the family of d versus D curves for ~~10%~~ typical experimental ~~variation~~ uncertainties in the ~~given~~ respective material parameter.

As seen in Figure 3, the errors in the DMI measurement are highest in the low DMI regions. How strongly the domain width varies with the DMI depends on how important the DMI is with respect to other parameters in determining the domain wall energy and its relative strength with respect to the stray field energy. In films where magnetostatics dominate, i.e., where the DMI energy is weaker, the DMI extraction shows larger error. When the DMI strongly influences the domain sizes (e.g., the region with $D > 1$ mJ/m^2), the error in extraction of DMI is lower.

The saturation magnetization is one of the strongest influences on estimated DMI as can be seen in Figure 3a since d depends on the square of M_S (*19*). Increasing M_S serves to increase magnetostatic energy thereby decreasing the domain size. A 10% 10% change in M_S would result in $\sim$ 50% error in estimation of DMI for the same d. The influence of M_S on the extracted D depends also on other parameters, such as its relative importance compared to K_U. In the experimental films studied in the previous section, the variation in D with M_S is significantly lower while the variation of D with K_U is much stronger as shown by the inability to obtain a fit without accounting for the anisotropy variation with changing Pt thickness. Figures 3b and 3c show the variation in D with uncertainties in K_U and A_{ex}, respectively. For the film parameters chosen, the variation in extracted D is smaller for these parameters. Both K_U and A_{ex} serve to increase domain wall energy and therefore increase the remanent domain sizes. However, a 10% error in K_U and 20% error in A_{ex} gives $<$ 20% error in estimated D. This is because d depends on the square-root of K_U and A_{ex}.

In the next section, we apply the analytical model (model 3) to measure DMI in sputtered multilayer magnetic thin films.

3 Measurement of DMI in experimental films

We measure DMI for two films, one similar to ~~that which has exhibited~~ the skyrmion ~~lattices~~ material in references (*5*, *27*), with inversion asymmetry, and the second with similar layer thicknesses as the first one, but with the same non-magnetic material at the top and bottom of the magnetic layer, i.e., with inversion symmetry, and hence an expected $D = 0$. For both films, we show that the measured DMI indeed agrees with expected values from theory and values obtained by other authors for similar films. We also find that the film growth mechanism imposes a variation in anisotropy with the thickness of the film, which is important to account for in the extraction of DMI. The two films chosen have different magnetic materials, CoFeB and Co, respectively, as well as a range of film thicknesses. The different magnetic materials chosen show the applicability of our technique of extracting DMI over a wide range of magnetic parameters and thicknesses.

Multi-layer thin films were deposited with the stacking structure: Ta(3 nm)/[Pt(2.5 - 7.5 nm)/$Co_{60}Fe_{20}B_{20}$(0.8 nm)/MgO(1.5 nm)]$_{13}$/Ta(2 nm) and Ta(3 nm)/[Pt(2.5 - 7.5 nm)/Co(0.8 nm)/Pt(1.5 nm)]$_{13}$/Ta(2 nm). Henceforth, they are referred to as the asymmetric and symmetric films, respectively. The deposition was done on Si(100) substrates with 50 nm thermally-grown SiO_2, at room temperature, with a base pressure of $\sim 3 \times 10^{-8}$ Torr, and at Ar pressure of 4.7 mTorr. The CoFeB

and MgO layers were deposited by rotational RF sputtering while the Ta and Co layers were deposited by rotational DC magnetron sputtering. Pt was deposited as a wedge where the thickness of the Pt layer was systematically varied from 2.5 nm to 7.5 nm, via stationary DC magnetron sputtering, across a lateral distance of 76.2 mm. The distance from the sputtering gun determined the thickness profile of the deposited Pt film.

Domains were imaged in the as-prepared and AC-demagnetized states using MFM with low moment CoCr magnetic tips. The AC-demagnetization process served to reorient the domains from labyrinth to stripe-like (Figure 4b-d) and ensured that the domain pattern thus obtained was the lowest energy configuration. Domain widths were quantified from the Fourier transform ~~FT~~ of 10×10 μm^2 MFM images (such as those shown in Figure 4b-d and Figure 6b-d) taken at different Pt thicknesses along the wedge. Figure 5b and Figure 7b show the domain size variation as a function of scaling factor for the asymmetric and symmetric films, respectively. Domain sizes decrease with increasing f for both films, as expected from theory and simulations.

Figure 4a shows a schematic of the asymmetric multilayer film with the gradient of the wedge exaggerated for clarity. Each substrate was cleaved into 12 rectangular pieces with each piece corresponding to a different average Pt thick-

ness along the wedge. The variation of Pt thickness on each piece was ~ 8 %. Easy- and hard-axis hysteresis loops were measured for every piece using Vibrating Sample Magnetometry (VSM). The saturation magnetization, M_S, was averaged across different Pt thicknesses and measured to be $6.9 \pm 0.2 \times 10^5$ A/m for the asymmetric stack. ~~One can also see that~~ Domain widths monotonically increase with increasing Pt thickness (Figure 4b-d) due to relatively weaker magnetostatic interaction as the separation between magnetic CoFeB layers increases.

~~Figure 4e-g show the variation in the shape of hysteresis loops of the asymmetric stack with changing Pt thickness. The multilayer film in the region of the thickest Pt layer (Figure 4g) shows a butterfly easy-axis hysteresis loop (typical of multi-layer magnetic films with stripe domains) (*28*, *29*) and a linear hard-axis loop. As Pt thickness is decreased, the easy-axis hysteresis loops get more and more sheared while the hard-axis hysteresis loops get more and more S-like (Figure 4g-e). This variation in hysteresis loop shape can be understood from the increase in density of magnetic layers with decreasing Pt thickness. As the magnetic layers come closer to each other, the interaction between them increases, resulting in a stronger magnetostatic coupling which is manifested as more sheared hysteresis loops with higher saturation fields (*24*).~~

Figures 4e-g show the FT of the domain patterns in 4b-d, respectively. Since

the domains are aligned vertically, the FTs show single peaks on the x-axis for Figures 4b,c. The FT intensity was averaged along the y-axis for Figures 4e,f and radially averaged for Figure 4g. The peak intensity was fit to a Gaussian function as in Figures 4h-j to determine the domain widths and their error bars.

For the asymmetric film we found that the anisotropy energy measured from the area between easy- and hard- axes hysteresis loops, K_{hys}, varies with the thickness of the Pt layer (Figure 5a). K_{hys} in magnetic thin films is related to the uniaxial anisotropy, K_U, as

$$K_{hys} = K_U - \frac{\mu_0 M_S^2}{2}; \tag{3}$$

K_{hys} represents the energy difference between saturating the magnetic film in the easy direction and the hard direction, which is the definition of the total anisotropy in the film irrespective of the equilibrium domain structure and thickness of the film (*30*). For multilayer magnetic films, Equation (3) is valid for the unscaled quantities, i.e., energy (area) or magnetization per unit magnetic volume (and not total volume of all the layers). If the interfacial contribution to anisotropy were independent of the Pt layer thickness, then one would expect K_{hys} to be independent of f in our thickness-graded multi-layer film since the magnetic layer thickness, T, remains constant throughout the wedge.

Experimentally, we find instead a variation of K_{hys}, which is well approximated phenomenologically by a second order polynomial. The origin of this strong variation in anisotropy with Pt thickness is unclear, but we suggest that it might arise as a manifestation of the film growth mechanism (directional deposition of Pt as opposed to rotational sputtering which gives a more uniform layer) which could induce variations in grain size or roughness with changing thickness of the Pt layer (*31*, *32*).

Figure 5b shows a plot of domain sizes obtained from MFM images as a function of f for the asymmetric film. The error bars correspond to the variation in domain sizes as measured from the uncertainty in the Gaussain fits to peak spatial frequency in the FT of the MFM images. We fitted these data to ~~the full domain wall energy model~~ model 3 described in the previous section. To do so, a model curve for domain spacing versus f was computed using the dependence of domain wall energy (Equation (1)) on f, using the experimentally-determined M_S and a second-order polynomial that accounts for the dependence of K_U on f. We assumed here an exchange constant $A_{ex} = 10^{-11}$ J/m (*5*), which will impact the magnitude of the extracted DMI but not the general analysis presented here. Note that other methods to extract DMI, such as those discussed in the Introduction, other than the ones (*12*, *13*) based on Brillouin Light Scattering (BLS), must

also assume a value for exchange constant since there is no reliable experimental measurement for A_{ex}. The curve was then fitted to the data using D as the only free fitting parameter. We note that if a single value of K_U is used for all values of f in the model, a consistent fit to the data cannot be obtained. The blue curve in Figure 5b shows the best fit using linear least squares optimization. An optimized value of $D = 1.6 \pm 0.2$ mJ/m^2 is obtained. To calculate the error in estimated D, M_S was varied within the measured error range, and A_{ex} and K_U were varied by 20 % each. All three quantities were varied in a Gaussian distribution around their expected values with distribution widths equal to the uncertainties in their estimation. The standard deviation of the resulting D values is shown as the error in D. The value of D measured using our method is similar to the D = 1.2 mJ/m^2 measured for [Pt(3 nm)/CoFe(0.6 nm)/MgO(1.8 nm)] film by domain wall motion experiments (*33*), and D = 1.8 mJ/m^2 measured for [Pt(4 nm)/CoFeB(1 nm)/MgO(2 nm)] by spin Hall switching experiments (*34*). D_{thr}, the minimum DMI required to exhibit Néel domain walls for this film, was calculated as in Ref. (*19*) and found to be < 0.1 mJ/m^2, which is significantly smaller than the D value extracted. This confirms that our film shows Néel domain walls. ~~with domain wall angle ψ = -90°. For low DMI films, the walls might be transient intermediate with ψ in between 0° and 90° or twisted (*35–37*). For such films, ignoring the film~~

~~thickness dependence of ψ and Δ might lead to significant error in extraction of DMI.~~

A large variation in anisotropy across the wedge (as seen in Figure 5a) suggests that the interface quality is varying in some systematic way across the wedge. This would indicate that DMI, which also comes from interfaces, might also vary systematically across the wedge. We also see that the fit to small scaling factors and large domain sizes in Figure 5b is poor. To consider the possibility of DMI variation across the wedge, DMI was calculated separately for different Pt thicknesses using their corresponding K_{hys} values (from Figure 5a). When calculated for each point on the wedge separately, DMI shows a trend following a similar pattern as that of K_{hys} as seen in Figure 5c varying within a range of 0.4 mJ/m^2. The small scaling factor data deviate the most from the fit value of D = 1.6 mJ/m^2 and show higher uncertainty in determination of D. The higher DMI for small scaling factors explains the smaller experimental domain sizes compared to the fit curve in Figure 5b . This shows that a single DMI value does not completely capture the interfacial DMI for the range of scaling factors in this film and a point by point analysis must be done.

A similar analysis was carried out for the symmetric film. Figure 6a shows a schematic of the symmetric multilayer film with the MFM images in Figures 6b-

d showing increasing domain widths with increasing thickness of the Pt wedge layer. The average saturation magnetization measured across 12 equally spaced locations on the wedge was measured to be $14.2 \pm 0.2 \times 10^5$ A/m. ~~The easy axis hysteresis loops showed a higher coercivity, as compared to the asymmetric film, with magnetization remanence ratio of 1. The hard axis loops were observed to be more linear (Figure 6e-g) than those of the asymmetric film across the full range of Pt thicknesses. The variation in the shape of the hysteresis loops across the symmetric wedge was seen to be much weaker in comparison with the asymmetric film, especially for the hard-axis loops.~~

Figures 6e-g show the FT of the domain patterns in Figures 6b-d, respectively. The domains are aligned vertically in Figure 6b and isotropically in Figures 6c,d. Therefore, the FT for Figure 6b shows single peaks on the x-axis, see Figure 6e. By contrast, the FT of Figures 6c,d show peaks of the shape of isotropic rings (Figures 6f,g). The FT intensity was averaged along the y-axis for Figure 4e and radially averaged for Figures 4f,g. For every FT, the peak intensity was fit to a Gaussian function, as in Figures 4h-j, to determine the domain width, d, and its error bar.

Figure 7 shows the DMI extracted for the symmetric sample. Here again, anisotropy variation was observed across the wedge (Figure 7a), which suggests a

variation in the interfacial anisotropy as a function of the Pt layer thickness.

Figure 7b shows that the symmetric film exhibits a decreasing domain size with increasing scaling factor. Note that the domain sizes for the symmetric film are larger than that of the asymmetric one (Figure 7b) implying a higher domain wall energy in the symmetric film. ~~The blue curve shows~~ The fit of the domain size versus scaling factor data to the model ~~with~~ yields $D = 0 \pm 0.1$ mJ/m^2. The uncertainty in D originates from the uncertainty in measured M_S and an assumed 20 % error bar in A_{ex} and K_U, where these parameters are varied in Gaussian distributions around their expected value. ~~D_{thr} for this film was calculated to be 0.03 mJ/m^2.~~ The D obtained is consistent with the concept of cancellation of interfacial DMI at the top and bottom interfaces in symmetric magnetic multilayer films (*38*, *39*).

Figure 7c shows the variation of DMI with scaling factor when DMI is calculated for each value of Pt thickness separately. The negative error bars terminate at 0 since we imposed a constraint to allow for only positive D values for our films. In our model, we extract only the magnitude of D. The handedness of DMI is taken into account via the domain wall angle. The large error bars show that it is difficult to extract D precisely for films with very small DMI. In films with small DMI, the walls might be intermediate with domain wall angle, ψ, in between 0°

and 90° or even twisted (*35–37*). For such films, ignoring the dependence of ψ and Δ on the film thickness might lead to significant error in extraction of DMI.

4 Summary

Measurement of DMI in ~~experimentally grown~~ single- and multi-layered magnetic thin films is necessary for assessing their potential as materials for skyrmionic memory and logic applications. In this work, we have shown that the DMI strength can be measured using well-established static magnetic characterization techniques. With the help of micromagnetic simulations, we show that the earlier models of stripe domains in demagnetized single and multi-layer magnetic films do not fully explain the domain spacing in magnetic thin films with DMI and Néel domain walls. ~~By ignoring the volume charges in domain walls,~~ An error of 72% is observed in the extraction of DMI in a micromagnetically simulated multilayer film when the analytical model used to extract DMI ignores volume charges in domain walls. ~~using analytical model expressions for the domain spacing.~~ After including volume charges in domain walls but ignoring the interaction of domain walls with each other, an error of 6% is observed. With the effects of finite domain wall width and inter-domain wall interaction (*19*), an error of only 1% is

observed in extracted DMI. DMI is then measured in two ~~experimentally grown~~ sputtered wedged magnetic multi-layer films. The film with asymmetrical top and bottom interface ~~The first one~~ shows a strong DMI with $D = 1.6 \pm 0.2$ mJ/m^2 and ~~second one~~ the film with symmetrical interfaces shows $D = 0 \pm 0.1$ mJ/m^2. The DMI extracted for both films is found to be consistent with values expected from theoretical predictions and observed in literature. The impact of uncertainties in measurement of three material parameters - M_S, A_{ex} and K_U - on the estimated DMI is used to calculate error bars. The DMI estimation is more accurate for films where the DMI strength is strong compared to the magnetostatic, anisotropic and exchange energies in the system. We also show that experimental variations in film deposition can lead to variations in DMI, possibly due to change in the quality of the interfaces between films. This work provides a fast and easy tool for experimental determination of DMI in multi-layer magnetic films with sheared hysteresis loops where experimental determination of DMI is complicated and comparison with micromagnetic simulations can be slow and inaccurate.

References

1. S. Emori, U. Bauer, S.-M. Ahn, E. Martinez, G. S. D. Beach, *Nature Materials* **12**, 611–6 (2013).

2. K.-S. Ryu, L. Thomas, S.-H. Yang, S. Parkin, *Nature Nanotechnology* **8**, 527–33 (2013).

3. T. Skyrme, *Nuclear Physics* **31**, 556–569 (1962).

4. A. Fert, V. Cros, J. Sampaio, *Nature Nanotechnology* **8**, 152–156 (2013).

5. S. Woo, K. Litzius, B. Krüger, M.-Y. Im, L. Caretta, K. Richter, M. Mann, A. Krone, R. M. Reeve, M. Weigand, P. Agrawal, I. Lemesh, M.-A. Mawass, P. Fischer, M. Kläui, G. S. D. Beach, *Nature Materials* **15**, 501–506 (2016).

6. W. Jiang, P. Upadhyaya, W. Zhang, G. Yu, M. B. Jungfleisch, F. Y. Fradin, J. E. Pearson, Y. Tserkovnyak, K. L. Wang, O. Heinonen, S. G. E. te Velthuis, A. Hoffmann, en, *Science* **349**, 283–286 (2015).

7. C. Moreau-Luchaire, C. Moutafis, N. Reyren, J. Sampaio, C. A. F. Vaz, N. V. Horne, K. Bouzehouane, K. Garcia, C. Deranlot, P. Warnicke, P. Wohlhüter, J.-M. George, M. Weigand, J. Raabe, V. Cros, A. Fert, *Nature Nanotechnology* **11** (2016).

8. S. Krause, R. Wiesendanger, *Nature Materials* **15**, 493–494 (2016).

9. H. Yang, A. Thiaville, S. Rohart, A. Fert, M. Chshiev, *Physical Review Letters* **115**, 267210 (2015).

10. M. Heide, G. Bihlmayer, S. Blügel, *Physica B: Condensed Matter* **404**, 2678–2683 (2009).

11. Y. Yoshimura, K.-J. Kim, T. Taniguchi, T. Tono, K. Ueda, R. Hiramatsu, T. Moriyama, K. Yamada, Y. Nakatani, T. Ono, *Nature Physics* **12** (2016).

12. J. M. Lee, C. Jang, B.-C. Min, S.-W. Lee, K.-J. Lee, J. Chang, *Nano Letters* **16**, 62–67 (2016).

13. H. T. Nembach, J. M. Shaw, M. Weiler, E. Jué, T. J. Silva, *Nature Physics* **11**, 825–829 (2015).

14. A. Hrabec, N. A. Porter, A. Wells, M. J. Benitez, G. Burnell, S. McVitie, D. McGrouther, T. A. Moore, C. H. Marrows, *Physical Review B* **90**, 020402 (2014).

15. S.-g. Je, D.-h. Kim, S.-C. Yoo, B.-C. Min, S.-b. Choe, K.-J. Lee, S.-b. Choe, *Physical Review B* **88**, 214401 (2013).

16. R. Lavrijsen, D. M. F. Hartmann, A. van den Brink, Y. Yin, B. Barcones, R. A. Duine, M. A. Verheijen, H. J. M. Swagten, B. Koopmans, *Physical Review B* **91**, 104414(8) (2015).

17. J. P. Pellegren, D. Lau, V. Sokalski, *Physical Review Letters* **119**, 027203 (2017).

18. K. An, D. R. Birt, C.-F. Pai, K. Olsson, D. C. Ralph, R. A. Buhrman, X. Li, *Physical Review B* **89**, 140405 (2014).

19. I. Lemesh, F. Büttner, G. S. D. Beach, *Physical Review B* **95**, 174423 (2017).

20. C. Kittel, *Reviews of Modern Physics* **21**, 541–583 (1949).

21. C. Kooy, U. Enz, *Philips Research Reports* **15**, 7–29 (1960).

22. Z. Malek, V. Kambersky, *Czechoslovak Journal of Physics* **8**, 416–421 (1958).

23. A. Suna, *Journal of Applied Physics* **59**, 313–316 (1986).

24. H. J. G. Draaisma, W. J. M. De Jonge, *Journal of Applied Physics* **621** (1987).

25. F. Büttner, B. Krüger, S. Eisebitt, M. Kläui, *Physical Review B* **92**, 054408 (2015).

26. A. Vansteenkiste, J. Leliaert, M. Dvornik, M. Helsen, F. Garcia-Sanchez, B. Van Waeyenberge, *AIP Advances* **4**, 107133(22) (2014).

27. F. Büttner, I. Lemesh, M. Schneider, B. Pfau, C. M. Günther, P. Hessing, J. Geilhufe, L. Caretta, D. Engel, B. Krüger, J. Viefhaus, S. Eisebitt, G. S. Beach, *Nature Nanotechnology* **12**, 1040–1044 (2017).

28. O. Hellwig, A. Berger, J. B. Kortright, E. E. Fullerton, *Journal of Magnetism and Magnetic Materials* **319**, 13–55 (2007).

29. D. M. Donnet, K. M. Krishnan, Y. Yajima, *Journal of Physics D: Applied Physics* **28**, 1942–1950 (1995).

30. M. T. Johnson, P. J. H. Bloemen, F. J. a. D. Broeder, J. J. D. Vries, *Reports on Progress in Physics* **59**, 1409–1458 (1999).

31. S. U. Jen, Y. D. Yao, Y. T. Chen, J. M. Wu, C. C. Lee, T. L. Tsai, Y. C. Chang, *Journal of Applied Physics* **99**, 053701(5) (2006).

32. Y.-T. Chen, C. Chang, *Journal of Alloys and Compounds* **498**, 113–117 (2010).

33. S. Emori, E. Martinez, K.-J. Lee, H.-W. Lee, U. Bauer, S.-M. Ahn, P. Agrawal, D. C. Bono, G. S. D. Beach, *Physical Review B* **90**, 184427 (2014).

34. C.-F. Pai, M. Mann, A. J. Tan, G. S. D. Beach, *Physical Review B* **93**, 144409(7) (2016).

35. I. Lemesh, G. S. D. Beach, *Physical Review B* **98**, 104402 (2018).

36. Y. Dovzhenko, F. Casola, S. Schlotter, T. X. Zhou, F. Büttner, R. L. Walsworth, G. S. Beach, A. Yacoby, *Nature Communications* **9**, 1–7 (2018).

37. W. Legrand, J.-Y. Chauleau, D. Maccariello, N. Reyren, S. Collin, K. Bouzehouane, N. Jaouen, V. Cros, A. Fert, *Science Advances* **4**, eaat0415 (2018).

38. P. P. J. Haazen, E. Murè, J. H. Franken, R. Lavrijsen, H. J. M. Swagten, B. Koopmans, *Nature Materials* **12**, 299–303 (2013).

39. J. Cho, N.-H. Kim, S. Lee, J.-S. Kim, R. Lavrijsen, A. Solignac, Y. Yin, D.-S. Han, N. J. J. van Hoof, H. J. M. Swagten, B. Koopmans, C.-Y. You, *Nature Communications* **6**, 7635 (2015).

Figures

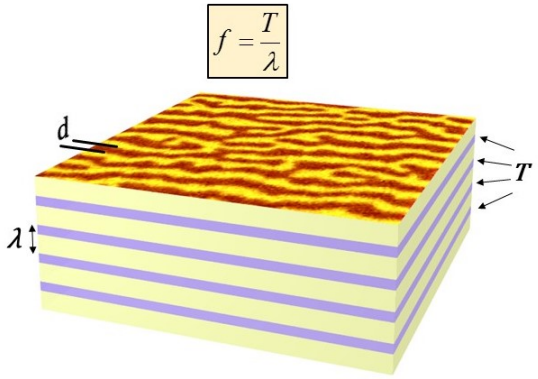

Figure 1: Schematic of magnetic multilayer film with stripe domains of width, d. The purple layers are magnetic films with thickness T, while the cream layers are non-magnetic. The thickness of each repeating set of layers is λ. A key structural parameter is the scaling factor, f, defined as the ratio of thickness of each magnetic layer to the thickness of a repeating set of layers, T/λ.

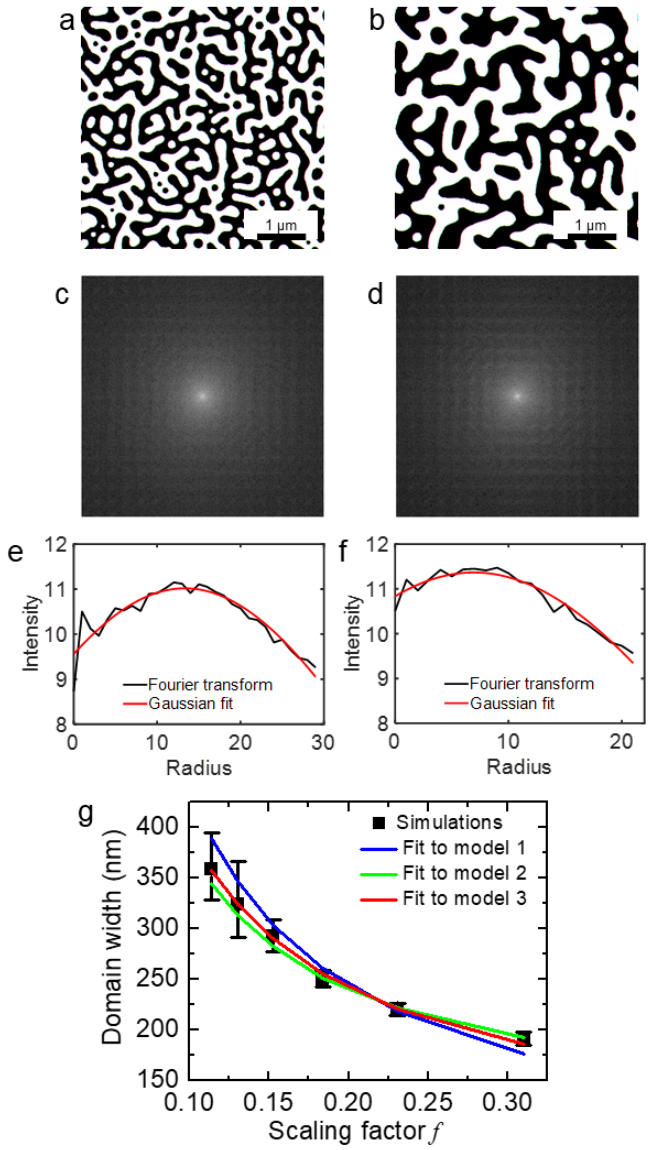

Figure 2: Measurement of DMI for micromagnetically simulated multi-layer film with DMI. a, b) 5×5 μm^2 images simulated with MUMAX^3 showing labyrinth domains for scaling factors of 0.31 and 0.11, respectively. c, d) Fourier transforms (FT) of images in a, b respectively. e, f) Gaussian fits to the peak of the radially averaged intensity of the Fourier transforms in c, d. g) Domain size as a function of scaling factor extracted from simulated images (black squares); fit to model 1 (blue curve), model 2 (green curve) and model 3 (red curve). The error bars on black squares correspond to errors in extraction of domain size from FT.

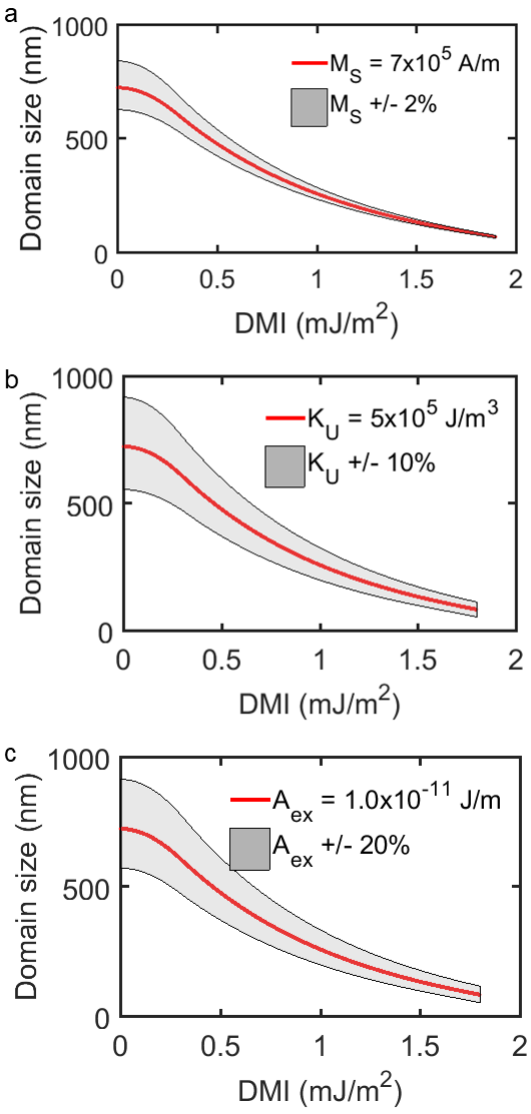

Figure 3: Domain size dependence on DMI and the effect of errors in different material parameters: a) saturation magnetization M_S, b) magnetic anisotropy K_U, c) exchange constant A_{ex}.

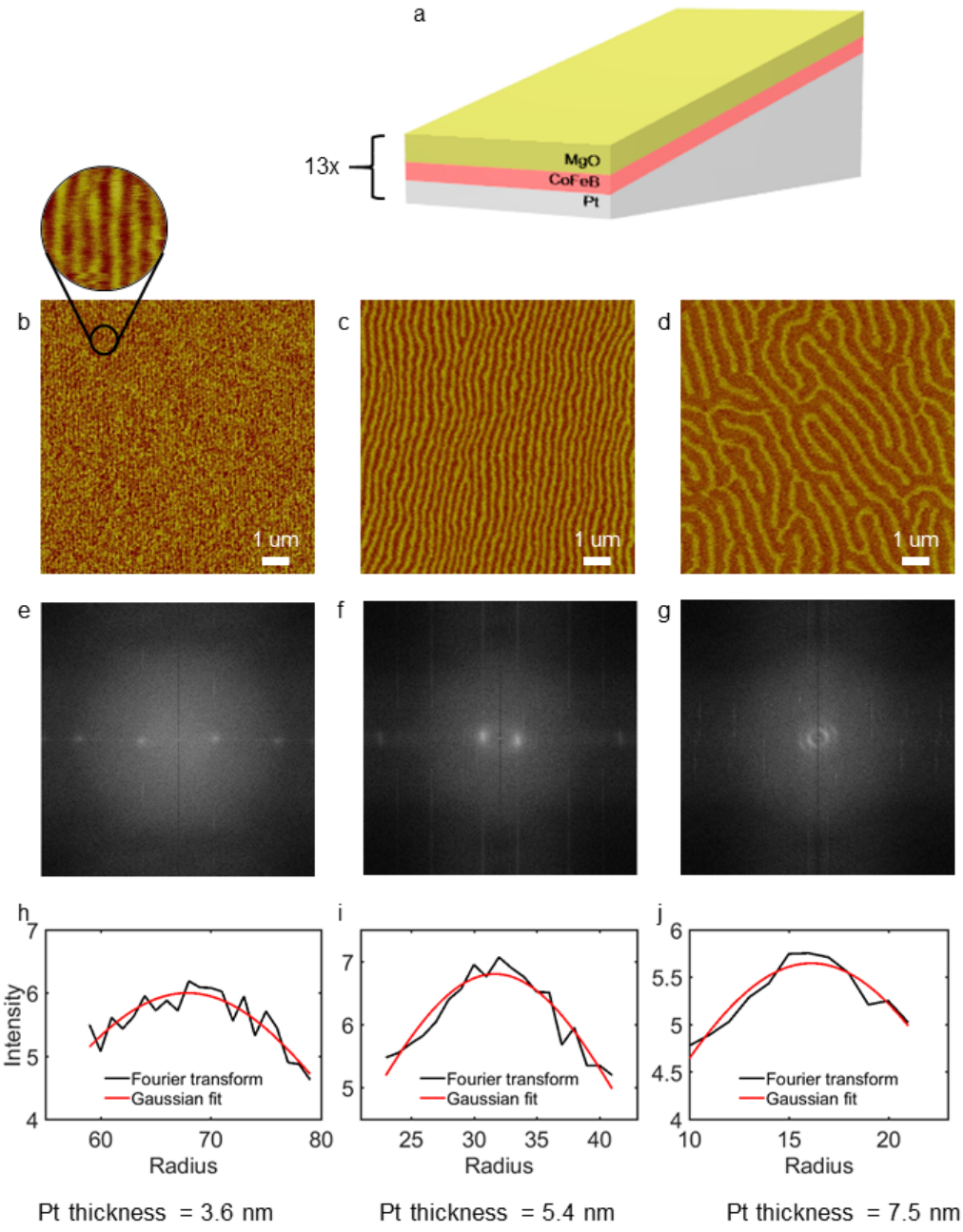

Figure 4: a) Schematic of the asymmetric multi-layer magnetic film with Pt layer wedged across the wafer. b) - d) 10×10 μm^2 MFM images showing stripe domains for Pt thicknesses 3.6 nm, 5.4 nm and 7.5 nm per repeating layer, respectively. Inset of b) shows a $10\times$ magnified image of stripe domains. e) - g) Fourier transforms of images in b) - d), respectively. h) -j) Gaussian fits to the frequency peaks in Fourier transforms in b) - d), respectively.

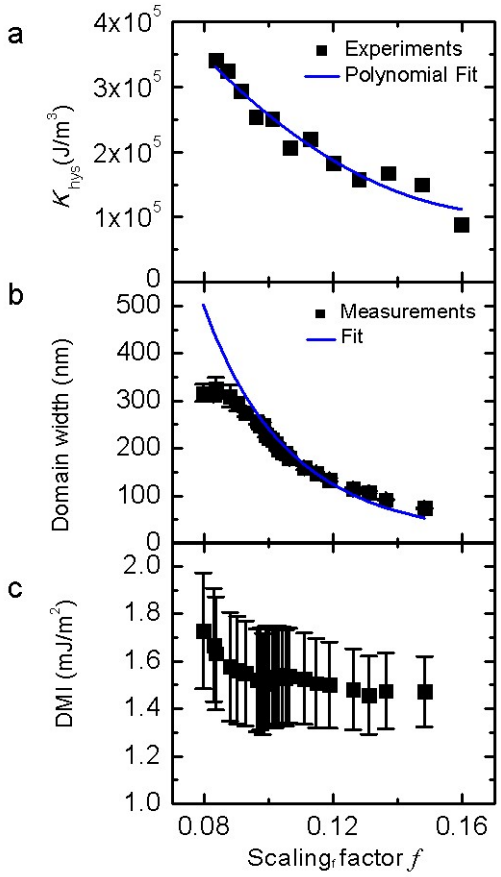

Figure 5: Measurement of DMI for the asymmetric film, $[Pt/CoFeB/MgO]_{13}$. a) Anisotropy obtained from hysteresis loops as a function of scaling factor, f, b) variation of domain size with scaling factor, f, showing fit with model 3 with D as fitting parameter (blue), c) D calculated separately for different scaling factors.

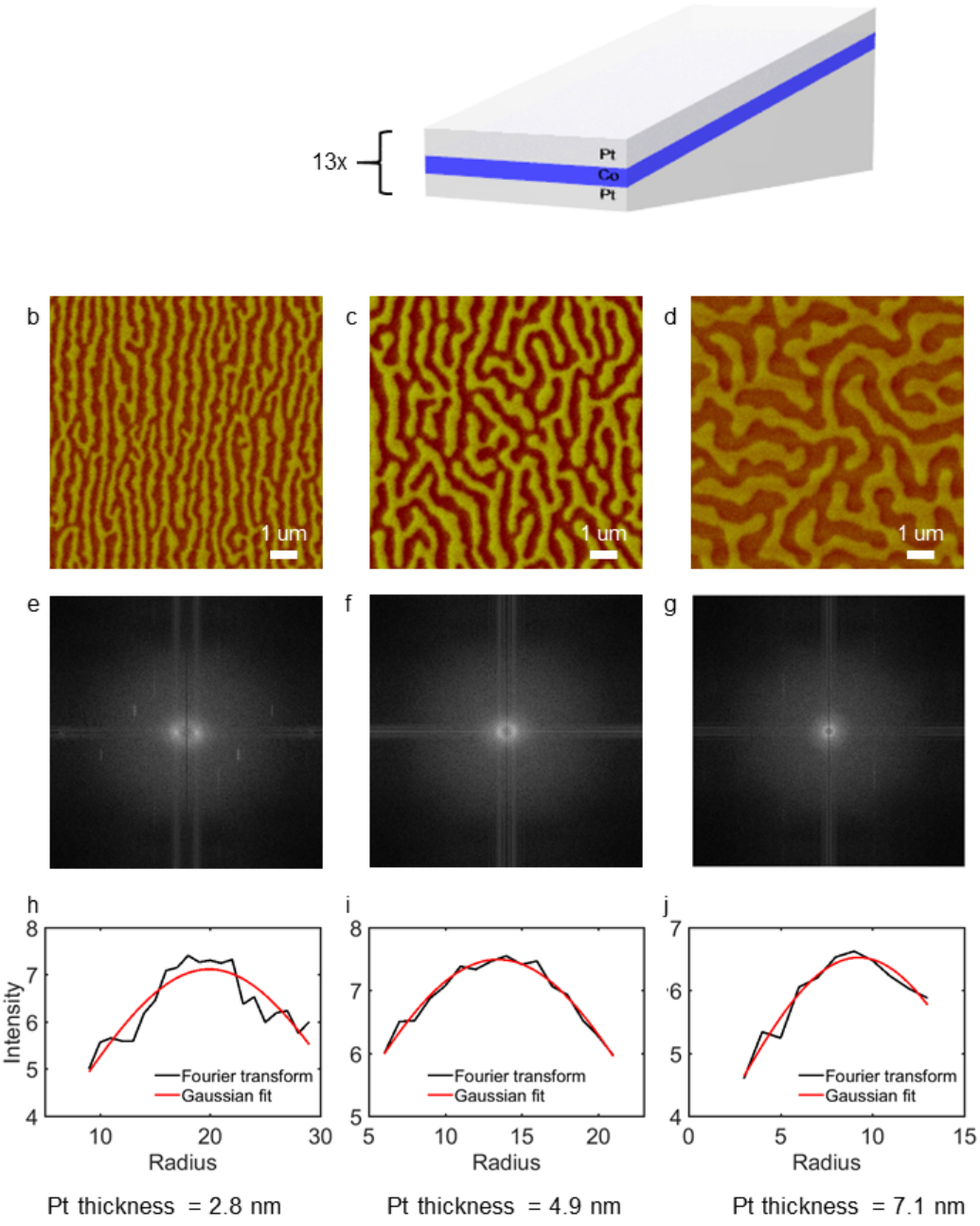

Figure 6: a) Schematic of the symmetric multi-layer magnetic film with Pt layer wedged across the wafer. b) - d) 10×10 μm^2 MFM images showing stripe domains at different Pt thicknesses. Fourier transforms of images in b) - d), respectively. h) -j) Gaussian fits to the frequency peaks in Fourier transforms in b) - d), respectively.

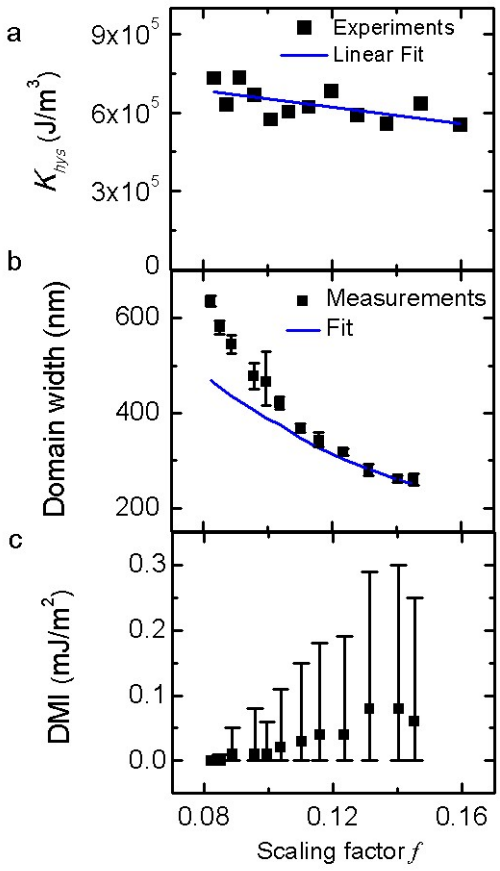

Figure 7: DMI calculation in the symmetric film, $[Pt/Co/Pt]_{13}$. a) Anisotropy obtained from hysteresis loops as a function of scaling factor, f. b) Variation of domain sizes obtained from MFM images (black squares) with scaling factor, f, showing fit with model 3 (blue curve). c) D calculated separately for different scaling factors.